Applied Catalysis B: Environmental 234 (2018) 213–222

Contents lists available at ScienceDirect

Applied Catalysis B: Environmental

journal homepage: www.elsevier.com/locate/apcatb

One-pot synthesis of sulfur and nitrogen codoped titanium dioxide nanorod arrays for superior photoelectrochemical water oxidation

Dinsefa M. Andoshe[a,b,1], Kanghoon Yim[a,1,2], Woonbae Sohn[a,c,1], Changyeon Kim[a], Taemin Ludvic Kim[a], Ki Chang Kwon[a], Kootak Hong[a], Seokhoon Choi[a], Cheon Woo Moon[a], Seung-Pyo Hong[a], Seungwu Han[a,*], Ho Won Jang[a,*]

[a] Department of Materials Science and Engineering, Research Institute of Advanced Materials, Seoul National University, Seoul 08826, Republic of Korea
[b] Materials Science and Engineering, Adama Science and Technology University, Adama, Ethiopia
[c] Energy & Environmental Division, Korea Institute of Ceramic Engineering & Technology (KICET), Jinju, Gyeongnam 52851, Republic of Korea

ARTICLE INFO

Keywords:
Titanium dioxide
Codoped
Photoelectrochemical water oxidation
Sulfur
Nitrogen

ABSTRACT

Despite its abundant, nontoxicity and photochemical stability, titanium dioxide shows low solar water oxidation performance due to low photogenerated carrier transport and wide optical band gap, which results in substantially low photogenerated carrier density that impair the solar to hydrogen conversion efficiency. Herein, highly enhanced water oxidation performance of high-aspect-ratio TiO_2 nanorods doped with dual heteroatoms, sulfur and nitrogen, for photoelectrochemical solar water oxidation is demonstrated. The codoped TiO_2 NRs have shown enhanced optical absorption coefficient due to the induced impurities energy states near to the top of the valance band and result in a red shift in the optical absorption edges. Consequently, a 2.82 $mAcm^{-2}$ photocurrent density at 1.23 V vs. RHE is obtained from the sulfur and nitrogen codoped TiO_2 nanorods, and pristine TiO_2 nanorods photoanode shows 0.7 $mAcm^{-2}$. The applied bias photon-to-current conversion efficiency and external quantum efficiency of the codoped TiO_2 nanorods are 1.49% and 97.0% at λ = 360 nm and 0.69% and 19.1% at λ = 370 nm for pristine TiO_2 nanorods, respectively. Our study offers experimental and theoretical evidence for codoping of sulfur and nitrogen improve the optical and electrical properties of TiO_2 for efficient photoelectrochemical solar water oxidation.

1. Introduction

Titanium dioxide is one of the most researched semiconductors for solar energy conversion devices, including solar water splitting (SWS) [1–3]. Although efforts have been made to tune the optical and electronic properties of TiO_2 in order to enhance the charge generation, transport, and transfer efficiency without suppressing the photochemical stability, TiO_2 is yet at the rear position in the race of *n*-type semiconductors for solar water splitting due to a slight improvement in the aforementioned drawbacks of TiO_2 [4,5]. Various routes and mechanisms have been developed to regulate the optical and electrical properties of TiO_2 for efficient photoelectrochemical solar water oxidation [4,6]. For example, thermal treatment of TiO_2 under high oxygen deficient environment results in oxygen vacancies and form shallow donors of energy levels which are near to the conduction band of TiO_2. The intentionally introduced impurity energy states can tune the optical properties of the TiO_2 nanostructure and show a red shift in the optical absorption that enhances the charge generation efficiency of the photoanode [7,8]. Similarly, doping of anions such as N [9–13], C [14], S [15,16], or cations e.g. Cu [11], Nb [17], W [18], Fe [19], Co [20], Cr [21], Mn [22] and surface coating with precious metals [23], can improve the optical, electrical properties and the photoelectrochemical performances of TiO_2. Furthermore, dual heteroatom doping of TiO_2 with carbon and tungsten has shown improved photoelectrochemical (PEC) water oxidation performance due to the enhancement of the photogenerated charge carriers transport and transfer efficiency of the host material [18]. However, a substantial enhancement of the photocurrent density at the 1.23 V vs. RHE was not observed from co-catalyst free TiO_2 photoanodes due to the high surface and bulk recombination of photogenerated carriers, low photogenerated charge carrier separation and collection [18,24].

The theoretical calculation and experimental studies have shown

* Corresponding authors.
E-mail addresses: hansw@snu.ac.kr (S. Han), hwjang@snu.ac.kr (H.W. Jang).
[1] These authors contributed equally to this work.
[2] Present address: Korea Institute of Energy Research, Daejeon 34129, Republic of Korea.

https://doi.org/10.1016/j.apcatb.2018.04.045
Received 16 October 2017; Received in revised form 5 February 2018; Accepted 18 April 2018
Available online 22 April 2018
0926-3373/

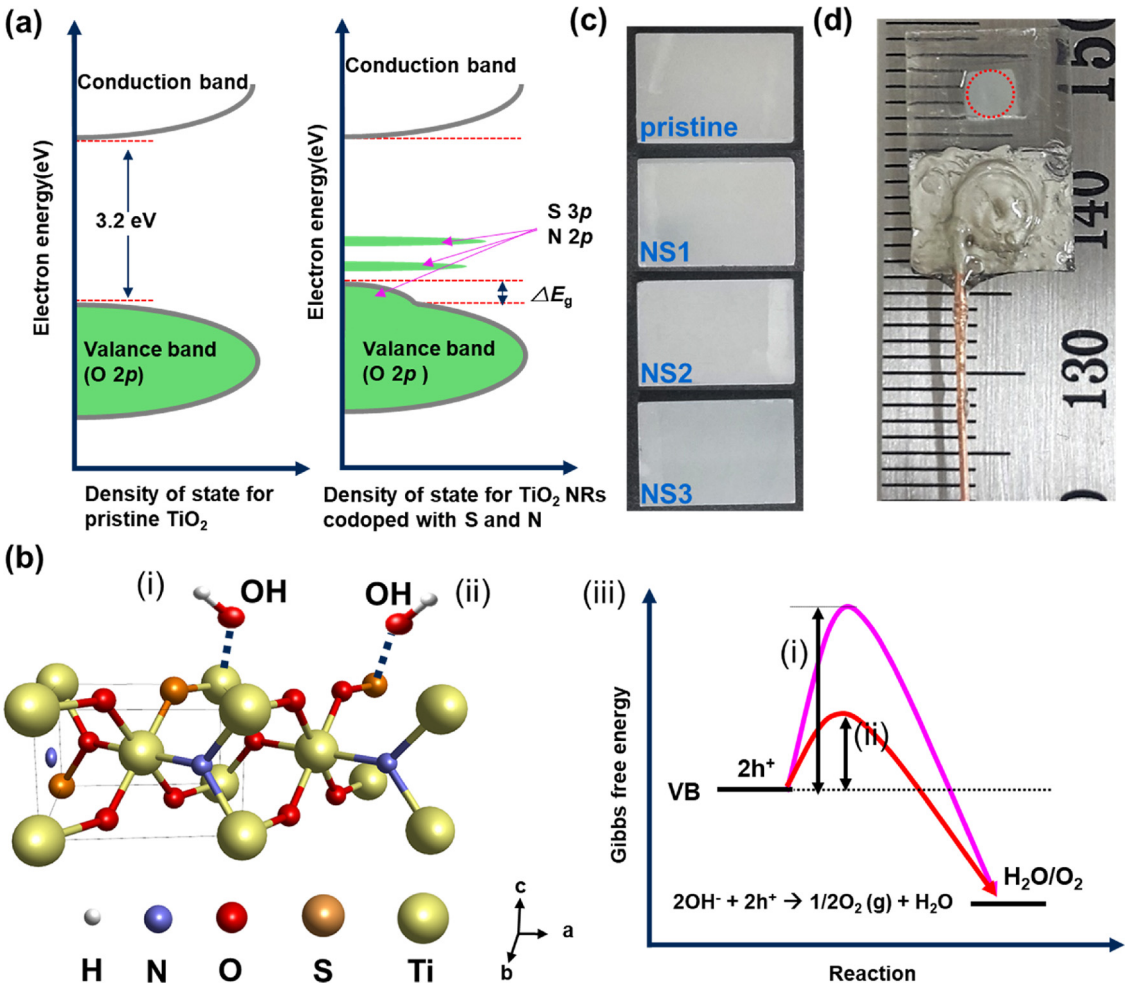

Fig. 1. (a) Schematic of expected density of state (DOS) for pristine and codoped TiO_2 NRs with sulfur and nitrogen. (b) Schematic illustration of hydroxide ions adsorption on the surface of (i) pristine TiO_2 NRs with titanium ion, (ii) codoped TiO_2 NRs with sulfur ion, respectively, and (iii) activation energy for oxygen evolution reactions for pristine TiO_2 NRs (red curve) and codoped TiO_2 NRs (blue curve). (c) Optical image of synthesized TiO_2 NRs codoped with different concentration sulfur and nitrogen. (d) Optical image of a prepared photoanode for photoelectrochemical measurements. (For interpretation of the references to color in this figure legend, the reader is referred to the web version of this article.)

that the codoping of TiO_2 with nonmetals can tune the optical and electrical properties of TiO_2 imposing impurities energy states near to the top of the valance band [24–26], as shown in Fig. 1(a). The optical band gap narrowing of TiO_2 codoped with sulfur and nitrogen could be due to the mixing of the partially filled N 2*p* and S 3*p* with the O 2*p* states and/or forming local states [27]. Nitrogen can be a substitutional (N_O, nitrogen replace oxygen) and/or interstitial dopant in the TiO_2 [28]. Sulfur can have several different charge states in the TiO_2 such as S^{-2}, S^{4+}, and S^{6+}: the most probable anionic sulfur (S^{-2}) when the sulfur atom substitutes the oxygen atom, the cationic sulfur (S^{4+}) when the titanium atom of TiO_2 is substituted by the sulfur atom, and the cationic sulfur (S^{6+}) when the formation of sulfate occurs [29]. Both the anionic and cationic sulfur states can act as optically active centers and catalytically active surface sites in the TiO_2 [30]. Fig. 1(b) shows a schematic for the adsorption of hydroxide ions (i) on the titanium and (ii) sulfur atoms at the surface of TiO_2 in the alkaline solution. Proton can transfer from the photoanode to the hydroxide ion with the lower activation energy for TiO_2 doped with sulfur than pristine TiO_2, as shown in Fig. 1(b) (iii), since the sulfur dopant can act as an effective adsorption site for the hydroxide ion in TiO_2 [26]. Likewise, the optical absorption edge of S doped TiO_2 could shift toward the visible light wavelength due to intentionally induced energy states. However, there are no experimental and theoretical studies that substantially verify the impact of codoping sulfur and nitrogen in the optical, electronic and photoelectrochemical water splitting properties of TiO_2.

Therefore, this work demonstrates the influence of dual heteroatom doping sulfur and nitrogen in the optical, electrical and photoelectrochemical properties of TiO_2 using both experimental and theoretical calculations. The details hydrothermal facile synthesis procedure is presented in the method section and illustrated in Fig. S1. We have studied the impact of codopant precursor concentration in the photoelectrochemical performance of TiO_2 (S, N) NRs photoanode and identified the optimum dopant precursor concertation.

The photoelectrochemical performance of codoped TiO_2 (S, N) NRs is found to be larger than the pristine TiO_2 NRs photoanode. Moreover, the linear sweep voltammograms (LSV) measurement shows the optimum current density 2.82 $mAcm^{-2}$ for the codoped TiO_2 (S, N) NRs photoanode at 1.23 V vs. RHE, which is much higher than the pristine TiO_2 NRs photoanode, 0.7 $mAcm^{-2}$. The outperform PEC performance of codoped TiO_2 (S, N) NRs over pristine TiO_2 NRs is attributed to the improvement of optical charge carrier generation and charge carriers transport in the TiO_2 (S, N) NRs photoanodes. Additionally, the measured chronoamperometry of codoped TiO_2 photoanode at 1.23 V vs. RHE for ~47 h has confirmed that the photochemical stability of TiO_2 is not impaired by the dual heteroatom doping of sulfur & nitrogen. To corroborate the experimental findings, theoretical calculation was conducted using first-principles density functional theory and verified the effect of N-doping, S-doping and (S, N)-codoping in the TiO_2. The

theoretical calculation reveals that dual heteroatom doping can decrease the dopant formation energy and enhance the optical absorption coefficient of TiO_2 NRs. Therefore, our study of codoped TiO_2 NRs with sulfur and nitrogen can contribute to the rapidly growing research field of the development of efficient PEC photoanode for solar water oxidation.

2. Experimental

2.1. Synthesis of codoped TiO_2 NRs on FTO/glass and photoanode preparation

The codoped TiO_2 NRs have grown on the FTO/glass using hydrothermal synthesis method with precursors DI-water, HCl and tetrabutyl titanate solutions with the amount of 25 ml and 25 ml, 0.8 ml, respectively [31]. Different amounts of sulfamic acid from 5 mg to 15 mg as a source of nitrogen and sulfur were added. The precursors were added sequentially as follows: DI-water, HCl, sulfamic acid and tetrabutyl titanate to a glass beaker and stirred vigorously using magnetic stirrer until the cloudy color changed to colorless as shown in Fig. S1(a). Subsequently, the solutions were transferred to a teflon beaker (100 ml) in which the FTO/glass was placed at the bottom keeping the active side faced up as shown in Fig. S1(b). The teflon beaker which had the precursor solution and the substrate, FTO/glass, was inserted into the autoclave and sealed properly as shown in Fig. S1(c). Subsequently it was cooked for four hours at 180 °C in an oven and kept inside until the temperature reached room temperature as shown Fig. S1(c). The synthesized codoped sample was removed from the teflon and rinsed repeatedly using DI-water and subsequently annealed at a temperature of 350 °C for half an hour in the ambient air condition. The temperature for annealing was ramped up at the rate of 5 °C/min until it reached the final temperature of, 350 °C. The sample was kept inside the furnace until the annealing temperature reached 140 °C and then was removed from the furnace.

Additionally, N-TiO_2 NRs by adding 5.0 gm urea to the solution containing TiO_2 precursor and S-TiO_2 NRs by sulfurization of TiO_2 NRs using tube furnace and 5 mg sulfur powder were synthesized.

We have prepared six different TiO_2 NRs photoanodes, four with different amounts of sulfamic acid precursor, as a source of both sulfur and nitrogen, to identify the optimum codopant concentration of H_3NSO_3 and designated as: sample one (pristine) which contain 0.0 mg of sulfamic acid, sample two (SN1) a 5 mg, sample three (SN2) a 10 mg, and sample four (SN3) a 15 mg, and the remaining two photoanodes were N-TiO_2 NRs and S-TiO_2 NRs to identify the effect of individual element to the PEC performance of TiO_2 NRS. Afterward, all the synthesized NRs using a blade from the FTO/glass substrate except ~10.0 m m^2 area were removed. A copper wire was connected using silver past to the conductive side of FTO/glass for the collection of majority charge carriers. The conductive part of the photoanodes except for the tail of the copper wire and a 9.74 mm^2 photoactive part, i.e., the area that was exposed to the electrolyte, repeatedly covered by transparent nail polish. To cure the TiO_2 (N, S) NRs photoanodes which were covered with nail polish are kept in the ambient air for a couple of hours, then the photoanodes become ready for PEC measurement as shown in Fig. 1(d).

2.2. Materials characterization

The morphologies of the synthesized pristine and codoped TiO_2 NRs were investigated using field emission scanning electron microscopy (FESEM: MERLIN compact, JEOL). The phase crystallinity of both pristine and codoped TiO_2 NRs was observed with high-resolution transmission electron microscopy (JEM-2100F, JEOL) and X-ray diffractometer (Bruker Miller Co., D8- Advance). The codopant distribution and elemental mapping were analyzed with high resolution X-ray photoelectron spectroscopy (Kratos AXIS-His) and scanning transmission electron microscope coupled with energy dispersive X-ray spectroscopy (JEM-2100F, JEOL). To measure EDS line scan, thick TiO_2 (S, N) NRs were synthesized [32] and a nanorod was cut at an arbitrary position to obtain the distribution of sulfur and nitrogen in the bulk and at the surface of TiO_2 NRs. The EDS line scan data of TiO_2 (S, N) NRs were obtained from the cross section of the cut nanorod and the EDS line scan was measured by FESEM. To identify the consequences of codopant, nitrogen and sulfur, in the optical properties of TiO_2 NRs, UV–vis absorption spectra were measured with wavelengths ranging from 300 nm to 800 nm. To measure the electrical properties of the synthesized samples a shadow mask with a hole diameter of 200 μm was taped on the top of the samples and subsequently, a silver metal contact was deposited using an electron-beam evaporator (KVE-E2004L) at the surface of the masked samples as shown in Fig. S5(a) inset. The current-voltage measurements were conducted at room temperature using a probe station with two probe tips. Afterward, the conductances of pristine and codoped TiO_2 NRs samples were calculated.

2.3. Photoelectrochemical measurement

The photoelectrochemical properties of both pristine and codoped TiO_2 NRs were measured using computer controlled potentiostat (IVIUM Technologies, nSTAT). All the PEC measurement were performed with NaOH electrolyte (pH = 13.6), single compartment cuvette and three electrodes configuration such as, the prepared photoanode, Ag/AgCl electrode and graphite rod were used as working, reference and counter electrode respectively. A Xe arc lamp was used as a light source and calibrated to 100 $mWcm^{-2}$ using a standard silicon photodiode at the sample location. In all of the linear sweep voltammograms measurements, the photoanodes were anodically polarized at the scan rate of 20 mV/sec during both illumination and in the dark measurement. The measured potential V vs. Ag/AgCl were converted to reference hydrogen electrode (RHE) using the following Eq. (1),

$$V_{RHE} = E + E_{Ag/AgCl} + 0.059 \times pH \quad (1)$$

where E is applied potential vs. Ag/AgCl and $E_{Ag/AgCl}$ is 0.21 V vs RHE and V_{RHE} is the applied potential vs. RHE.

The IPCE, which is equivalent to external quantum efficiency, of the samples was measured at applied bias potential of 0.23 V vs. Ag/AgCl using computer controlled monochromator (MonoRa150) and an amplifier for photocurrent detection. The electrochemical impedance spectroscopy (EIS) was measured at 0.23 V vs. Ag/AgCl with respect to open circuit potential (OCP) and sweeping in the frequency range of 350 K Hz – 0.1 Hz with an AC amplitude of 10 mV. The EIS Nyquist curves were fitted to equivalent circuit using Zplot 2x software. To obtain the carrier concentration of the synthesized TiO_2 NRs, Mott-Schottky (M–S) measurements were performed at frequency of 1 kHz with a sweeping bias potential of 0.0 V–0.8 V vs Ag/AgCl using the same electrodes and electrolyte presented somewhere above. The carrier density was calculated using a M–S Eq. (2),

$$\frac{1}{C_{sc}^2} = \frac{1}{\varepsilon_r \varepsilon_0 A^2 e N_D}\left(E - E_{fb} - \frac{kT}{e}\right) \quad (2)$$

where C_{sc} space charge layer of the sample, ε_r relative permittivity of the sample, $\varepsilon_{r.TiO_2}$ is 170 [8], ε_0 permittivity of free space, A is active surface area of the measured sample, e is an elementary charge, N_D is carrier density of the measured photoanode, E is applied potential, E_{fb} is flat band potential of the measured material, k and T are Boltzmann constant and temperature, respectively.

The applied bias photon-to-current conversion efficiency (ABPE) measurement was performed using two electrodes, the prepared photoanode and platinum wire without any sacrificial donor/acceptor and single compartment cuvette. The bias potential (V_b) was applied between the working electrode and the counter electrode (Pt wire). The resulting ABPE value were obtained using the following Eq. (3),

$$\mathrm{ABPE} = \left(\frac{|J(\mathrm{mAcm^{-2}})| \times (1.23 - |V_b|)(V)}{I(\mathrm{mW\,cm^{-2}})}\right) \times 100\,\% \quad (3)$$

where J is the photocurrent density, I the incident illumination intensity (100 mWcm^{-2}) and V_b the bias potential, 1.23 V is a thermodynamic water splitting potential.

2.4. Theoretical calculation

Vienna Ab initio Simulation Package (VASP) [33] with projector augmented-wave (PAW) potentials is used for the density functional theory (DFT) calculations. We employ the generalized gradient approximation (GGA) for the exchange-correlation function. The energy cutoff of the plane-wave basis set to 400 eV and the 3 × 3 × 4 Monkhorst-pack **k**-point sampling is used for primitive cell of rutile TiO_2. For the defect calculation, we use 144-atom supercell with Γ-only **k**-point which corresponds to same **k**-point density compared to primitive cell. The dopant formation energy is calculated using following Eq. (4),

$$E_{\mathrm{For}}(\mathrm{doped}, q) = E_{\mathrm{tot}}(\mathrm{doped}, q) - E_{\mathrm{tot}}(\mathrm{perfect}) + \sum N_i\mu_i + q(\varepsilon_F + \varepsilon_{\mathrm{VBM}}) + E_{\mathrm{corr}} \quad (4)$$

where E_{For} is the formation energy of dopant, E_{tot} is the total free energy of supercell, q is the charge state, N_i and μ_i are the number and chemical potential of the chemical species i, and ε_F is the Fermi energy with respect to the valence band maximum energy ($\varepsilon_{\mathrm{VBM}}$). E_{corr} is the correction energy to remove spurious electrostatic interactions among image charges in the repeated cells. For E_{corr}, we use FNV correction considering the anisotropic dielectric constant [34,35]. We use conventional DFT calculation for the calculation of defect formation energies, so the band gap is underestimated. For optical-property calculations, we adopt HSE06 hybrid functional with 0.25 of the fraction of Fock exchange which result in the band gap of 3.16 eV. We use the 2 × 2 × 2 Monkhorst-pack **k**-points and large number of unoccupied bands are included to obtain well-converged result. The frequency dependent dielectric matrix is obtained from the calculation and absorption coefficeint is calculated using Eq. (5),

$$\alpha_{\mathrm{abs}} = \frac{2\omega k(\omega)}{c},\ k(\omega) = \sqrt{\frac{\sqrt{\varepsilon_1^2 + \varepsilon_2^2} - \varepsilon_2}{2}} \quad (5)$$

where α_{abs} is the absorption coefficient, ω is the frequency, $k(\omega)$ is refractive index, c is speed of light, and ε_1 and ε_2 represent real and imaginary part of dielectric function. The partial density of states are obtained by PAW projector using the result of optical propery calculcation.

3. Result and discussion

The optical image of the synthesized samples with different amount of sulfamic acid (H_3NSO_3) (see method section for detail) such as 0.0 mg, 5.0 mg, 10.0 mg, 15.0 mg for pristine, SN1, SN2 and SN3 specimens are shown in Fig. 1(c), respectively. The color of the synthesized TiO_2 NRs specimens has slightly changed from dull white to light yellow while the amount of codopant precursor has increased. Fig. 1(d) shows the photoanode with the active area encircled by the red dotted line, and the details preparation of the photoanode is presented in the method section. The pristine TiO_2 NRs and codoped TiO_2 (S, N) NRs have an average length of 6.7 μm and 150 nm in diameter as revealed by scanning electron microscopy (SEM) and transmission electron microscopy (TEM) shown in Fig. 2 and Fig. S2. The high aspect ratio (length/diameter) nanorods have short photogenerated carrier diffusion length than planar TiO_2 [36]. The TEM and selected area electron diffraction patterns (SAED) measurement reveal that the crystalline phase and the lattice parameter of both pristine and codoped TiO_2 NRs do not show any noticeable difference as shown in Fig. 2. It was found that both pristine and codoped TiO_2 NRs are a rutile phase. The lattice plane of {110} and {001} for both pristine and codoped TiO_2 NRs were clearly visible and the plane spacing parameter d was calculated for both samples.

The lattice spacing d_{ijk} are found to be d_{001} = 0.296 nm and d_{110} = 0.325 nm for (001) and (110) planes, respectively, as shown in Fig. 2(c) and (g). It is plausible to assume that the low concentration of the codopant in the TiO_2 specimens and the negligible difference in the atomic radius between the codopant and oxygen atom will show indistinguishable crystalline phase and lattice parameter [9].

Crystallinity and growth habit analysis of the synthesized pristine and codoped TiO_2 NRs was conducted using X-ray diffraction measurement. All samples were found to be a rutile structure of TiO_2 (as confirmed by TEM analysis) with different lattice plane peak intensities, i.e., (002) > (101) > (110) as shown in Fig. 2(e). The intensity difference suggested that the preferred growth direction could be [001] for both pristine and codoped TiO_2 NRs. Moreover, the intensity of (110) facet for codoped TiO_2 NRs is smaller than the intensity of (101) facet while the intensity of (110) facet for pristine TiO_2 NRs is greater than the intensity of (101) facet.

The reason could be that the codopant in the TiO_2 NRs can exist in that facet and discourage the growth in the [110] direction while motivating the growth in the [101]. Energy dispersive spectroscopy (EDS) analysis revealed that nitrogen and sulfur dopants are uniformly distributed in the entire TiO_2 NRs, as shown in Fig. 2(i) and Fig. S3. The concentration of oxygen in the codoped TiO_2 NRs sample is slightly lower than that of pristine TiO_2 NRs as shown in Fig. S4. The observed low oxygen amount in the codoped TiO_2 NRs could be a result nitrogen and sulfur, which substituted the oxygen atom in the TiO_2 NRs [13].

To unveil the chemical states of the codopant (nitrogen and sulfur) in the TiO_2 NRs, high-resolution X-ray photoelectron spectroscopy (XPS) measurements were conducted as shown in Fig. 2(j)–(m). The deconvolution of the spectra shows that nitrogen has two peaks in the TiO_2 (S, N) NRs at the binding energy of 399.3 eV and 400.9 eV. The two N 1*s* peaks arise from a Ti-N and N–O bond due to the substitution of nitrogen for oxygen (N_O) and the existence of nitrogen atom in the interstitial sites, respectively, and these peak positions correspond to previous studies [37,38]. These peaks also observed in the Ti 2*p* and O 1*s* spectra. The interstitial nitrogen in the TiO_2 may serve as a potential recombination sites for photogenerated carriers [11]. Likewise, the S 2*p* spectrum has two peaks at 170 eV and 172 eV of binding energy; these two peaks may be attributed to the oxidation states of S^{4+} and S^{2-} for S atom in the TiO_2 NRs [15]. The anionic sulfur peak arise when the oxygen atom is substituted by the sulfur atom (S_O) and the cationic sulfur peak suggests the substitution of titanium atom with the sulfur atom (S_{Ti}).

The PEC performance of pristine and codoped TiO_2 NRs was measured and the LSV curves of all samples are presented in Fig. 3(a). It is known that the pristine TiO_2 NRs show low current density at 1.23 V vs RHE due to no absorption of the visible light wavelength and low charge carrier transport properties [10,39]. Similarly, our pristine TiO_2 NRs show a current density of 0.7 mAcm^{-2} at 1.23 V vs. RHE as shown in Fig. 3(a) (purple color). The obtained photocurrent density of pristine TiO_2 NRs is less than the theoretical predicted current density of TiO_2 [40]. However, all the codoped photoanodes samples, Fig. 3a (red, blue and green curves) exhibit an excellent PEC performance for water oxidation with current densities of 2.82, 2.45 and 1.7 mAcm^{-2} at 1.23 vs. RHE (V) for the SN1, SN2 and SN3 photoanodes, respectively. The SN1 photoanode has the highest photocurrent density among of all photoanodes, and more specifically it has four times higher photocurrent density than the pristine TiO_2 NRs photoanode at 1.23 vs. RHE (V). The possible reasons could be (i) the rate of charge generation has dominated the recombination rate (ii) the sulfur dopant provides catalytically active surface sites and facilitate the rate of adsorption and desorption of reactant and product, respectively. Furthermore, in general, the multi-element doping can employ to manipulate the density of photogenerated carriers and carrier kinetics of the host material; and

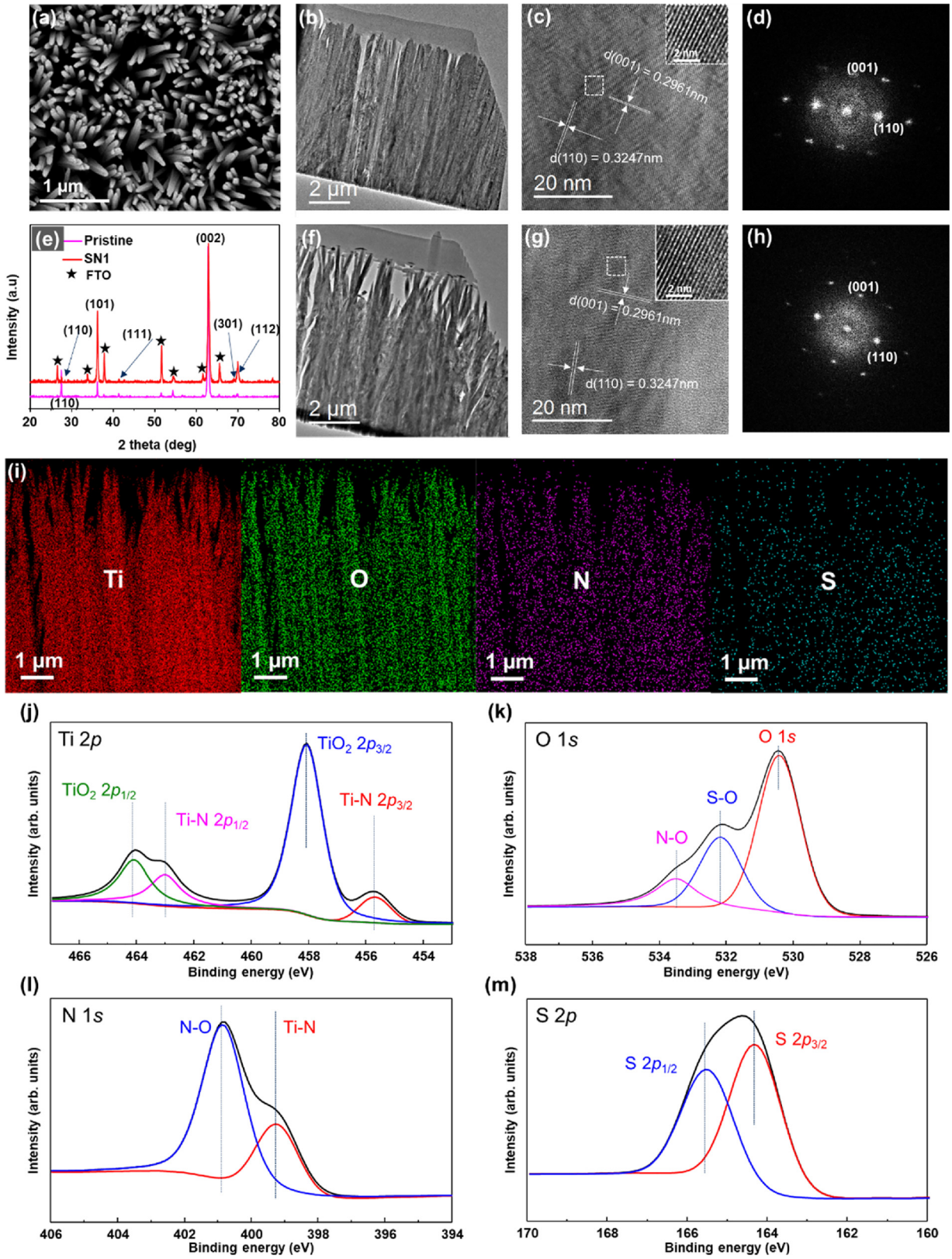

Fig. 2. SEM and TEM images of codoped and pristine TiO_2 NRs, the corresponding XRD, EDS and high resolution XPS analysis. (a) Planar view SEM image (b) cross-sectional TEM image for pristine TiO_2 NRs (c) High resolution TEM image for a pristine TiO_2 NRs. The inset is a magnified image for the selected region. (d) Selected area diffraction pattern of the pristine TiO_2 NRs. (e) XRD spectra of pristine TiO_2 NRs (purple curve) and codoped TiO_2 NRs (red line). (f) Cross-sectional TEM image of codoped TiO_2 NR. (g) High resolution TEM image of a codoped TiO_2 NR. The inset is a magnified image for the selected region. (h) Selected area diffraction pattern of the codoped TiO_2 NR. (i) Elemental mapping for titanium, oxygen, nitrogen and sulfur in the synthesized TiO_2 NRs sample by using STEM. (j)-(m) XPS analysis for Ti 2*p*, O 1*s*, N 1*s* and S 2*p* in the TiO_2 (S, N) NRs specimen, respectively. (For interpretation of the references to color in this figure legend, the reader is referred to the web version of this article.)

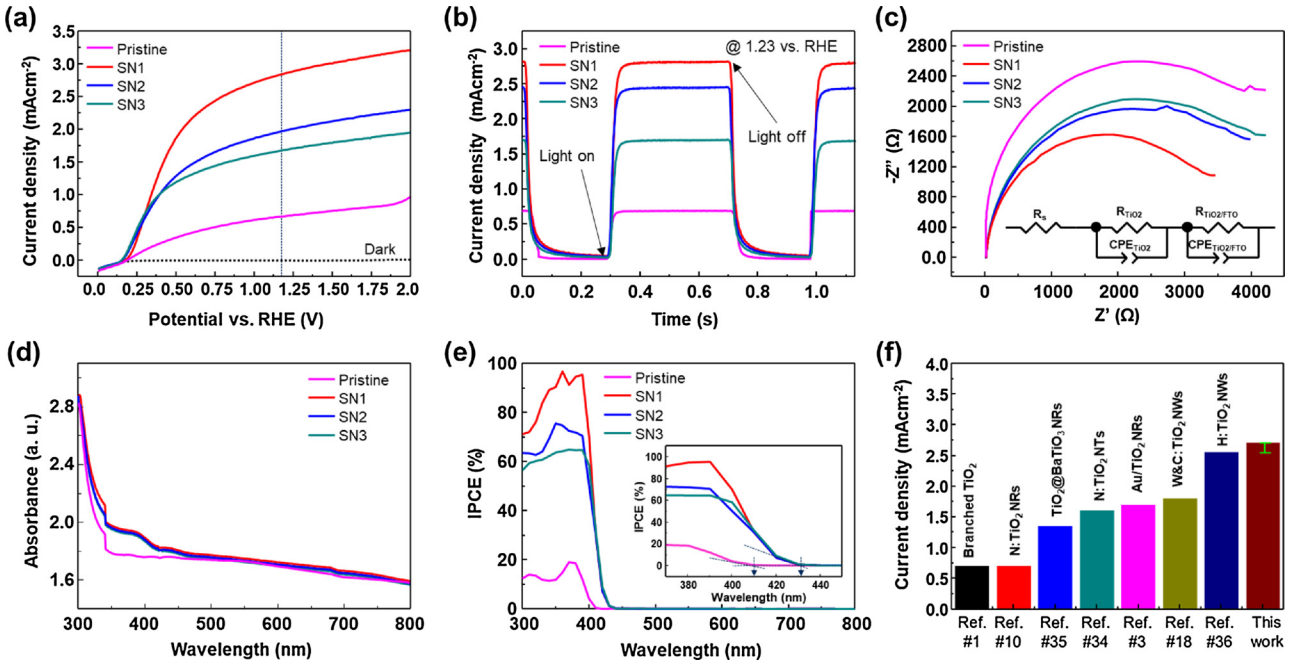

Fig. 3. Photoelectrochemical performance. (a) Linear sweep voltammograms of pristine and codoped TiO_2 NRs with different doping concentration. (b) The corresponding chronoamperometry of pristine and codoped TiO_2 NRs photoanodes at 1.23 mAcm^{-2}. (c) Nyquist plots for both pristine and codoped TiO_2 NRs samples and their equivalent circuit. (d) Optical absorption spectra of pristine and codoped samples. (e) External quantum efficiency of pristine and codoped TiO_2 NRs. (f) Comparing our result with recently published results. The green mark in the dark red bar (our photoanode) indicates the amount of photocurrent difference from the dark blue bar. (For interpretation of the references to color in this figure legend, the reader is referred to the web version of this article.)

this work has confirmed the effectiveness of codoping sulfur and nitrogen pairs to enhance the performance of the TiO_2 photoanode. The chronoamperometry of all samples was measured with chopped light with a 0.3 s time interval. The photocurrent curve behavior in the transient measurement is highly dependent on carrier accumulation and the rate of carrier recombination. While the light source was off, the photocurrents in all codoped samples, SN1, SN2 and SN3, were slowly reducing to zero as shown in Fig. 3(b). Therefore, the slow turnoff of current density in the codoped photoanodes attributed to the enhancement of carrier diffusion length.

Moreover, to verify the individual dopant, S and N, contribution to the PEC performance of TiO_2 NRs N-TiO_2 NRs and S-TiO_2 NRs were studied by doping a 5 mg of each nitrogen and sulfur containing the precursor to TiO_2. The LSV curves of the N-TiO_2 NRs and S-TiO_2 NRs were compared with SN1 and pristine photoanode as shown in Fig. S6. It has been observed that individual element can enhance the current density of the TiO_2 NRs photoanode, however, the codoped TiO_2 NRs photoanode is yet superior. The current density at 1.23 vs. RHE (V) of pristine TiO_2 NRs, N-TiO_2 NRs, S-TiO_2 NRs and SN1-TiO_2 NRs were 0.7, 1.1, 1.71 and 2.82 mAcm^{-2}.

The electrochemical impedance spectroscopy (EIS) of TiO_2 NRs photoanodes was measured to elucidate the charge transfer in the interface between electrode and electrolyte (R_{TiO2}); and between the synthesized TiO_2 NRs and FTO substrate ($R_{TiO2/FTO}$). The corresponding Nyquist plots have shown a single semi-circle which began at the origin as illustrated in Fig. 3(c). The fitted equivalent circuit element of the obtained Nyquist data consists of R_s, R_{TiO2}, $R_{TiO2/FTO}$ and constant phase elements (CPE). The corresponding analyzed circuit element values are presented in Table1. Despite the slight variation of R_s value of the photoanodes, such as pristine = 17.1, SN1 = 12.4, SN2 = 13.84 and SN3 = 13.8 Ωcm^2, the obtained series resistance (R_s) values have confirmed that the excellent photocatalytic performance of TiO_2 NRs. The charge transfer resistance at the electrode-electrolyte interface (R_{TiO2} (Ωcm^2)) in the SN1, SN2, SN3 and pristine photoanodes are 216.06, 362.33, 424.7 and 676 Ωcm^2 respectively.

Moreover, the charge transfer resistance at the TiO_2 NRs-FTO interface ($R_{TiO2/FTO}$ (Ωcm^2)) for the SN1, SN2, SN3 and pristine are 127.9, 192.85, 229.7 and 383.63 Ωcm^2, respectively. The codoped samples have smaller R_{TiO2} and $R_{TiO2/FTO}$ than the pristine TiO_2 NRs photoanode. Likewise, the electrical conductance of the TiO_2 NRs was found to be 6.23 × 10^{-12}, 3.9 × 10^{-8}, 2.65 × 10^{-9}, and 2.35 × 10^{-10} Sm^{-1} for the pristine, SN1, SN2, and SN3 samples, respectively, as shown in Fig. S5(a). The R_{TiO2} and $R_{TiO2/FTO}$ were increased and the conductance was decreased while the amount of codopant concentration increased these could be due to the enhancement of lattice and impurities scattering in the codoped TiO_2 NRs [41].

Table 1
Fitted charge transfer and transport resistance.

Photoanodes	R_s (Ωcm^2)	R_{TiO2} (Ωcm^2)	$R_{TiO2/FTO}$ (Ωcm^2)
Pristine TiO_2 NRs	17.1	676	383.63
SN1	12.4	216.06	127.9
SN2	13.84	362.33	192.85
SN3	13.8	424.7	229.7

To analyze the ability of the photoanodes to convert the input photons into output electrons, we measured the incident photon-to-current conversion efficiency (IPCE) of the photoanodes at a wavelength of 300 nm to 800 nm at 1.23 V vs. RHE as shown in Fig. 3(e). The IPCE values of the photoanodes are 19.1% at a wavelength of 370 nm, 97.0% at a wavelength of 360 nm, 75.7% at a wavelength 350 nm, and 65.1% at a wavelength of 370 nm for pristine, SN1, SN2, and SN3, respectively. The IPCE onset wavelength of the codoped samples, SN1, SN2, and SN3 is ~430 nm, shown in the inset of Fig. 3(e), corresponds to the optical band gap of 2.88 eV for codoped samples. The enhanced IPCE efficiencies in the UV region (wavelength < 400 nm) are highly related to the decrease of charge transfer and transport resistances in the TiO_2 (S, N) NRs photoanodes. Therefore, the photocurrent densities of the codoped samples partly accredited to the improvement of the carrier kinetics in the specimens. The UV visible absorption of all four samples was measured to identify the contribution of the

photogenerated charge carriers to the IPCE values of the photoanodes and it was found that the optical absorption of all codoped samples have shown a slight improvement of the entire wavelength of < 450 nm relative to the pristine TiO_2 NRs sample as shown in Fig. 3(d). It implies that the concentration of photogenerated electron-hole pairs is higher in the codoped samples, which has a role in the enhancement of IPCE value for the codoped samples. The calculated optical band gap of TiO_2 NRs using a UV visible absorption data and Tauc plot is 3.1 eV for pristine and 2.88 eV for all codoped TiO_2 NRs samples (SN1, SN2, SN3) as shown in Fig. S5(b), which is highly aligned with the estimated band gap using the IPCE onset wavelength. The decrease of the optical band gap of TiO_2 from 3.1 eV to 2.88 eV for codoped samples attributes to the formation of new defect energy states to the top of valance band of TiO_2 NRs due to the presence of nitrogen and sulfur.

In comparison with the current densities at 1.23 vs. RHE (V) of recently reported TiO_2 photoanodes without co-catalysts, in which their performance was improved by doping anions or/and cations [18,42], Au decoration [3], heterojunction [32]. Hydrogen treated [43], and morphology and surface engineering [1], and the current density of our codoped TiO_2 NRs photoanode is plotted in Fig. 3(f). The TiO_2 NRs photoanode codoped with nitrogen and sulfur was found to be superior to those photoanodes, particularly the SN1 photoanode has a 11.4% higher current density (which is indicated by green mark on the dark red bar) at 1.23 vs. RHE (V) than the hydrogen treated TiO_2 photoanode [43], which is considered as the best photoanode from co-catalyst free TiO_2 based electrodes that have been reported for PEC water oxidation.

The Mott-Schottky (M–S) measurement is performed to determine the effect of codopant in the carrier density of the TiO_2 NRs specimens. Consequently, the inverse squares of the capacitance of the space charge (C_{sc}) of the nanorods versus electrode potential V for all samples were plotted as shown in Fig. 4(a). The slope of M–S plots for all samples are positive and this suggests that the synthesized TiO_2 NRs samples are *n*-type semiconductors. Furthermore, the calculated carrier density of the TiO_2 NRs specimens are found to be 8.6×10^{17}, 6.9×10^{18}, 5.6×10^{18} and 3.68×10^{18} cm^{-3} for the pristine, SN1, SN2, and SN3 samples, respectively. From these values and the lattice parameters of TiO_2 crystals, it was confirmed that each dopant occupies a substitutional site per each 10 unit cells. The distance between the dopants is estimated to be about 4.4 nm along the a and b axis and 2.7 nm along the c axis. Because the distance between dopants is too close to each other, we could not observe the exact distance between dopants in the TEM-EDS analysis. But the dopants are uniformly distributed throughout the entire TiO2 nanorods based on the TEM-EDS images in Fig. 2.

The increment of carrier density in the codoped samples implies the improvement of charge carrier kinetics in the photoanodes. This is manifested by the enhancement of IPCE in the UV region and chopped light chronoamperometry measurement. Another main cause for the improvement of carrier density in codoped samples could be due to the red shift in optical absorption edge from UV (400 nm) to visible region (430 nm) that enhances the charge generation efficiency of the samples.

The applied bias photon-to-current conversion efficiency (ABPE) of the best performing photocathode, SN1, and pristine TiO_2 NRs were measured using the two electrode configuration experiment. The obtained current density using the two electrode configuration is lower than the three electrode experiment as shown in Fig. 4(b). The decrease in photocurrent density during two electrode experiment is attributed to the enhancement of the thermodynamic water splitting potential [40]. The calculated ABPE using Eq. (3) for pristine and SN1 was found to be 0.69% at maximum power point potential of, V_{mpp} = 1.35 V vs.

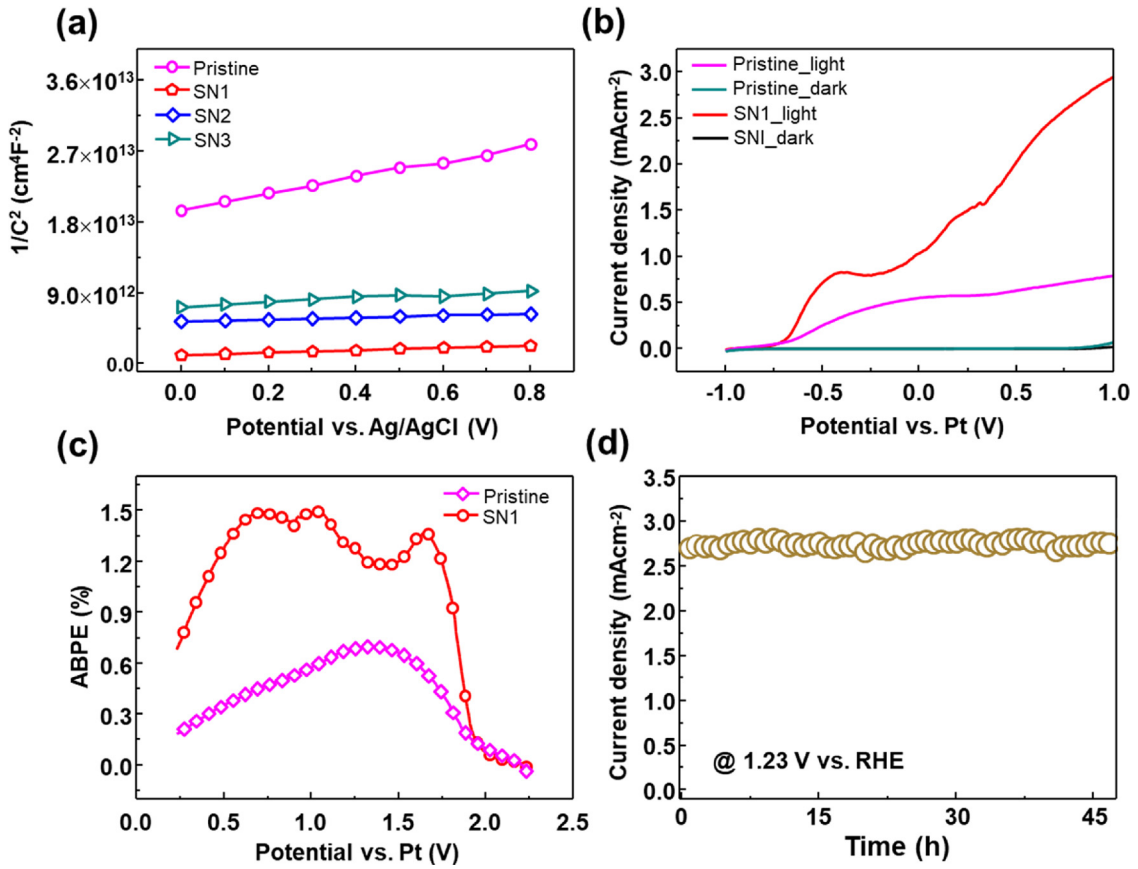

Fig. 4. Mott-schottky plot and Photoelectrochemical efficiency of the photoanodes. (a) Mott-schottky plot for pristine and codoped samples (SN1, SN2 and SN3). (b) Two electrode LSV curves of pristine and SN1 samples. (c) Applied bias photon-to-current conversion efficiency of pristine and SN1 samples. (d) Chronoamperometry measurement of the SN1 photoanode for long period of time.

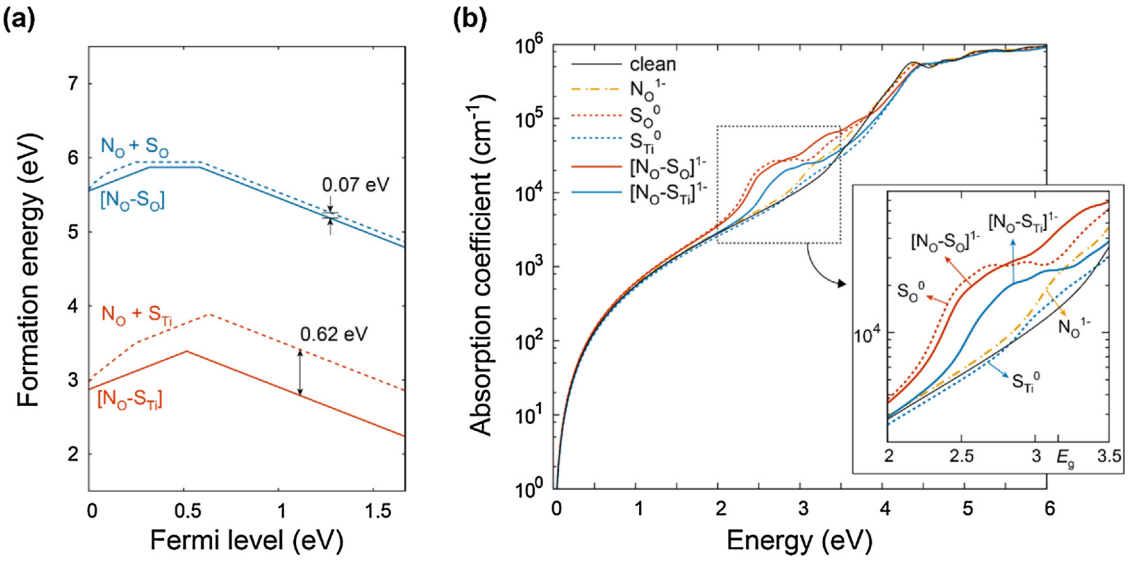

Fig. 5. (a) Calculated formation energies of defect complexes (solid line) compared to sum of each isolated dopants (dash line). Chemical potentials are determined from the assumption that chemical potential of oxygen is $E(O_2) - 1.5$ eV, which is arbitrarily chosen for the good visibility. GGA functional is used for the calculation. (b) Light energy versus absorption coefficient by HSE06 hybrid functional calculation. Absorption coefficient is shown in log scale. The region in the dashed square is magnified in the inset figure.

Pt electrode and 1.49% at 0.71 V vs. Pt electrode and illustrated in Fig. 4(c). We measured chronoamperometry of SN1 samples for an extended time to verify the photochemical stability of the codoped samples. The measured photocurrent density versus time curve shows that the SN1 sample is stable for more than 47.4 h without any noticeable degradation as shown in Fig. 4(d). The photoelectrochemical oxidation of water from codoped samples for an extended period of time confirms that the codoping of nitrogen and sulfur can't impair the intrinsic photochemical stability of TiO_2.

To gain a further understanding of codopant atom interaction with the host atoms and with each other a density functional theory (DFT) calculation were employed to discuss the dopant formation energies, optical properties and partial density of state (PDOS) of N-doped, S-doped, and (S, N)-codoped TiO_2 specimens (See Experimental Section for more computational details). The dopant formation energy calculation shows nitrogen is found to prefer oxygen substitutional site (N_O) while the cation substitutional site is very unstable. Interstitial nitrogen requires much higher formation energy compared to N_O in low oxygen partial pressures, but it becomes comparable to N_O as the formation energy of N_O increases with O_2 pressure. In the case of sulfur, both anion substitution and cation substitution can exist depending on the chemical environment. In high O_2 pressure region, titanium substitutional sulfur (S_{Ti}) is dominant while oxygen substitutional sulfur (S_O) takes the majority in oxygen deficient environment. These results well agree with our XPS analysis.

Therefore, the resulting defect chemical reactions, while both sulfur and nitrogen doped in the TiO_2, could be presented using the conventional Kroger-Vink notation (i)–(iii), Which fulfills the required conservation of mass, charge, and lattice site stoichiometry. While the N^{3-} substitute the O^{2-} lattice site in the TiO_2 one may describe the electronic defect as (i) and

$$N \xrightarrow{TiO2} TiTi0 + NO' + 1/2Oo0 + h0 \quad \text{(i)}$$

$$S \xrightarrow{TiO2} S_{Ti}^{0} + 2O_{O}^{0} \quad \text{(ii)}$$

$$S \xrightarrow{TiO2} S_{O}^{0} + Ti_{Ti}^{0} \quad \text{(iii)}$$

the charge has to be balanced by the addition of a hole. While S^{2-} and S^{4+} substitute oxygen lattice site (O^{2-}) and titanium lattice site (Ti^{4+}) in the TiO_2, respectively, the corresponding electronic defect chemical reaction can be described as (ii) and (iii).

To identify the codoping effect in terms of dopant stability, we compare the formation energy of defect complexes with the sum of isolated dopant formation energies as shown in Fig. 5(a); both defect complexes of N_O with S_O ($[N_O\text{-}S_O]$), and N_O with S_{Ti} ($[N_O\text{-}S_{Ti}]$) are more stable than sum of each isolated dopants. Especially for $N_O\text{-}S_{Ti}$, the formation energy is lowered by 0.62 eV as N_O and S_{Ti} interact when they are next to each other. This means codoping of nitrogen and sulfur can enhance the dopant stability and higher dopant concentration can be obtained compared to when they are doped separately. Since the binding energy gain of $[N_O\text{-}S_O]$ is much smaller (~0.07 eV) than for $[N_O\text{-}S_{Ti}]$, the concentration of $[N_O\text{-}S_O]$ in the TiO_2 NRs expected to be smaller. We note that the chemical potentials are chosen in Fig. 6(a) to provide better visibility for each defect complex, but the relative formation energies can be reversed depending on the chemical environment.

To compare the light absorption efficiency in visible light region, the absorption coefficient of each doped-TiO_2 are calculated in Fig. 5(b). Each absorption coefficient is calculated using the defective supercells containing each defect or defect complex, corresponding to 1 ~ 2 at. % of dopant concentrations. The charged states of each dopant or dopant complex are determined by assuming that the Fermi level is within the upper region from the mid gap position since undoped TiO_2 is an *n*-type semiconductor. First, it is shown that S_O° significantly increases absorption in the visible light region while N_O^{1-} and S_{Ti}° show almost no contribution in the energy window below 3 eV. However, in the case of $[N_O\text{-}S_{Ti}]^{1-}$, the defect complex from codoping makes significant increase of absorption coefficient in the visible light region, unlike the monoatomic (sulfur or nitrogen) dopant. This is because the interaction between N_O and S_{Ti} creates deep and localized states in $[N_O\text{-}S_{Ti}]^{1-}$ which facilitate the optical absorptions. On the other hand, the $[N_O\text{-}S_O]^{1-}$ does not show a significant difference from that of S_O°. As already shown in Fig. 5(a), the interaction between neighboring $N_O\text{-}S_O$ is weak, so the increase in the visible light region should be mostly contributed by S_O°.

These features also can be explained by the partial density of states (PDOS) of each defect configurations as shown in Fig. 6. The defect states of N_O^{1-} and S_{Ti}° are lying near the VBM while S_O°, $[N_O\text{-}S_O]^{1-}$ and $[N_O\text{-}S_{Ti}]^{1-}$ form the defect states around 1 eV above VBM. We confirm that the localized state above the VBM of $[N_O\text{-}S_O]^{1-}$ is mostly composed

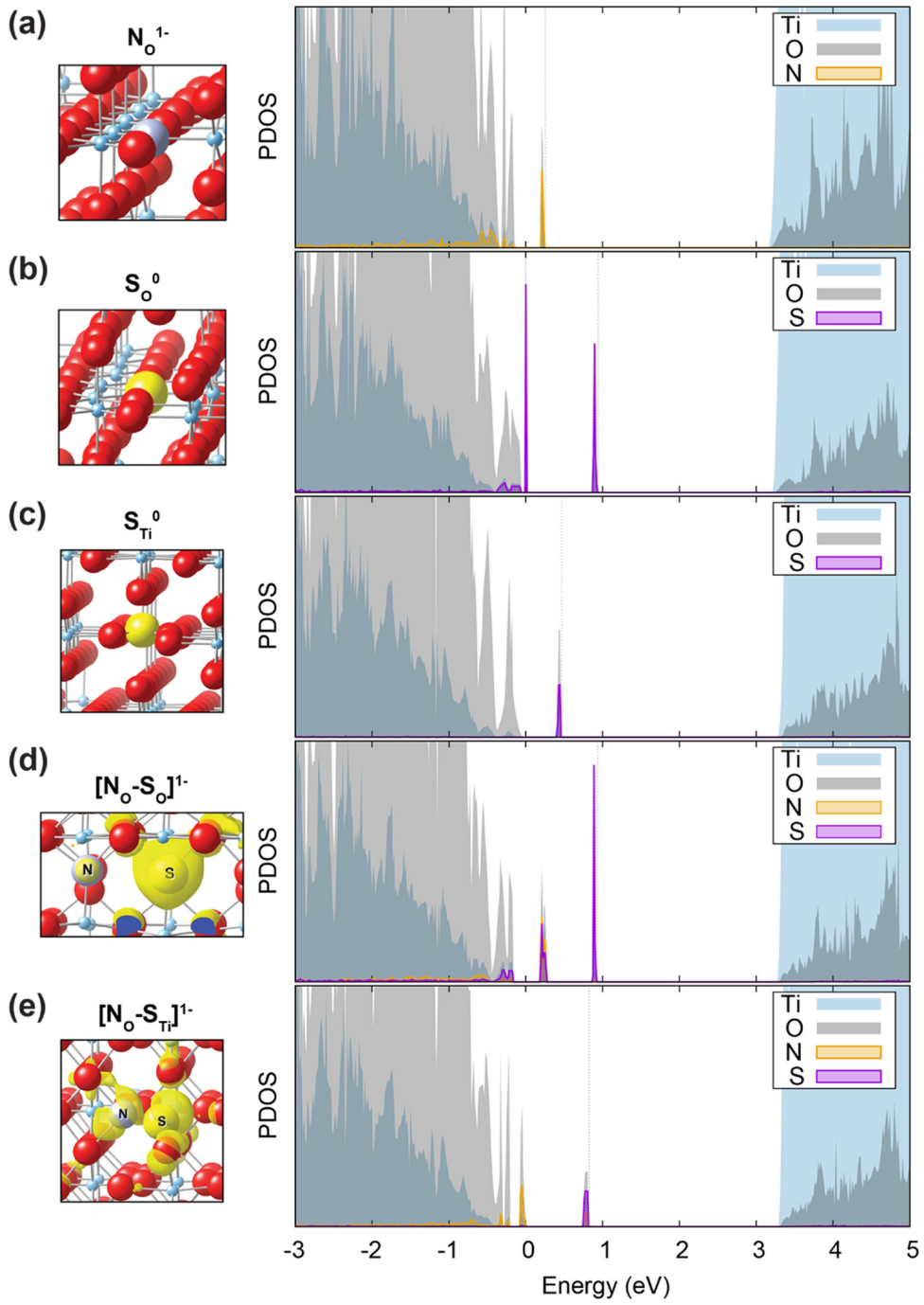

Fig. 6. (a) Dopant configurations and partial density of states (PDOS) (a) N_O^{1-}, (b) S_O°, (c) S_{Ti}°, (d) $[N_O\text{-}S_O]^{1-}$, and (e) $[N_O\text{-}S_{Ti}]^{1-}$. x-axis represents relative energy level from the VBM of bulk TiO_2 and grey-dashed line indicates the highest occupied levels of each defect. For (d) and (e), isosurface of highest occupied orbitals is shown in the dopant configuration.

with S 3*p* with negligible hybridization with N 2*p* that is also shown in the isosurface of the defect state in Fig. 6(d). Unlike $[N_O\text{-}S_O]^{1-}$, the defect state of $[N_O\text{-}S_{Ti}]^{1-}$ is made by hybridization of N_O^{1-} and S_{Ti}° as shown in Fig. 6(e). Since both S^{2-} (S_O°) and S^{4+} (S_{Ti}°) are present in our sample, both $[N_O\text{-}S_{Ti}]^{1-}$ and $[N_O\text{-}S_O]^{1-}$ contribute to the enhancement of the PEC performance of the photoanode.

The related photoreactivity of SN-TiO_2 NRs/FTO photoanode is demonstrated in the Fig. S7. The theoretical calculation confirmed that between the band gap of TiO_2 the hybrid localized defect states of S 3*p* and N 2*p* are observed. The enhanced current density in the SN-TiO_2 probably because the excitation takes place from the localized defect states of S 3*p* and N 2*p* using visible light as shown in Fig. S7. The photogenerated hole from the localized defect states of the S 3*p* and N 2*p,* and O 2*p* state of TiO_2 reduces the OH– ion and produce water and oxygen gas [44].

4. Conclusion

We studied TiO_2 NRs codoping with sulfur and nitrogen for PEC water splitting. We found that codoping nitrogen and sulfur can enhance the photocurrent density of TiO_2 photoanodes without suppressing the photochemical stability of titanium dioxide. The outperformance of codoped TiO_2 NRs photoanodes is due to the intentionally formed impurity energy states at the top of TiO_2 valence

band and enhanced charge transfer and transport properties of the host material. The PEC performance of codoped TiO_2 NRs photoanode is highly dependent on the concentration of codopant precursor. The PEC perforce was decreased when the codopant precursor concentration was increased. The optimum amount of codopant concentration nitrogen and sulfur, in the TiO_2 NRs shows a 2.82 $mAcm^{-2}$ current density at 1.23 V vs. RHE, which is four times higher than the pristine TiO_2 NRs photoanode, and 1.49% of applied bias-to-current conversion efficiency. Moreover, the codoped TiO_2 NRs photoanode can convert the incident photon to current with 97% efficiency in the UV wavelength region. The theoretical study suggests that the interaction between the dopant atoms (S, N) and the host material can enhance the dopant stability in TiO_2 due to the low dopant formation energy for the [N_O-S_{Ti}] defect complex. All codopant complex either [N_O-S_{Ti}] or [N_O-S_O] in TiO_2 can enhance the optical absorption coefficient in the visible light region. We have also demonstrated the partial density of states for all possible dopant configuration in the TiO_2 specimens to corroborate the optical absorption coefficient enhancement. Although our study only focuses on the codoping of nitrogen and sulfur in TiO_2 NRs, this approach can be extended to other codopants such as acceptor-acceptor, acceptor-donor and donor-donor pairs in the titanium dioxide photoelectrode to enhance the PEC water splitting performance.

Acknowledgements

This research was supported by the Basic Science Research Program [2017R1A2B3009135], the Future Material Discovery Program [2016M3D1A1027666], and the Nano Material Technology Development Program [2016M3A7B4910] through the National Research Foundation of Korea (NRF) and the International Energy Joint R&D Program [20168510011350] of the Korea Institute of Energy Technology Evaluation and Planning (KETEP).

Appendix A. Supplementary data

Supplementary material related to this article can be found, in the online version, at doi:https://doi.org/10.1016/j.apcatb.2018.04.045.

References

[1] I.S. Cho, Z. Chen, A.J. Forman, D.R. Kim, P.M. Rao, T.F. Jaramillo, X. Zheng, Nano Lett. 11 (2011) 4978–4984.
[2] (a) F.E. Osterloh, Chem. Mater. 20 (2008) 35–54;
(b) Z. Xu, M. Yin, J. Sun, G. Ding, L. Lu, P. Chang, X. Chen, D. Li, Nanotechnology 27 (2016) 115401;
(c) U. Diebold, Surf. Sci. Rep. 48 (2003) 53–229;
(d) Z. Li, Z. Zhou, G. Yun, K. Shi, X. Lv, B. Yang, Nanoscale Res. Lett. 8 (2013) 473.
[3] Y.-C. Pu, G. Wang, K.-D. Chang, Y. Ling, Y.-K. Lin, B.C. Fitzmorris, C.-M. Liu, X. Lu, Y. Tong, J.Z. Zhang, Y.-J. Hsu, Y. Li, Nano Lett. 13 (2013) 3817–3823.
[4] G.G. Bessegato, T.T. Guaraldo, M.V.B. Zanoni, Modern electrochemical methods, in: M. Aliofkhazraei (Ed.), Nano, Surface and Corrosion Science, INTECH, Croatia, 2014, p. 271.
[5] S.Y. Chae, P. Sudhagar, A. Fujishima, Y.J. Hwang, O.-S. Joo, Phys. Chem. Chem. Phys. 17 (2015) 7714–7719.
[6] (a) E. Barborini, A.M. Conti, I. Kholmanov, P. Piseri, A. Podestà, P. Milani, C. Cepek, O. Sakho, R. Macovez, M. Sancrotti, Adv. Mater. 17 (2005) 1842–1846;
(b) X. Chen, L. Liu, P.Y. Yu, S.S. Mao, Science 331 (2011) 746–750;
(c) D.-Y. Wang, C.-H. Li, S.-S. Li, T.-R. Kuo, C.-M. Tsai, T.-R. Chen, Y.-C. Wang, C.-W. Chen, C.-C. Chen, Sci. Rep. 6 (2016) 20397;
(d) Z. Zhang, P. Wang, Energy Environ. Sci. 5 (2012) 6506–6512;
(e) S. Cho, J.-W. Jang, K.-H. Lee, J.S. Lee, Appl. Mater. 2 (2014) 010703.
[7] X. Pan, M.-Q. Yang, X. Fu, N. Zhang, Y.-J. Xu, Nanoscale 5 (2013) 3601–3614.
[8] H. Wang, G. Wang, Y. Ling, M. Lepert, C. Wang, J.Z. Zhang, Y. Li, Nanoscale 4 (2012) 1463–1466.
[9] S.A. Ansari, M.M. Khan, M.O. Ansari, M.H. Cho, New. J. Chem. 40 (2016) 3000–3009.
[10] Z. Li, F. Wang, A. Kvit, X. Wang, J. Phys. Chem. C 119 (2015) 4397–4405.
[11] J. Su, Z. Li, Y. Zhang, Y. Wei, X. Wang, RSC Adv. 6 (2016) 16177–16182.
[12] J. Tang, A.J. Cowan, J.R. Durrant, D.R. Klug, J. Phys. Chem. C 115 (2011) 3143–3150.
[13] J. Lynch, C. Giannini, J.K. Cooper, A. Loiudice, I.D. Sharp, R. Buonsanti, J. Phys. Chem. C 119 (2015) 7443–7452.
[14] J.H. Park, S. Kim, A.J. Bard, Nano Lett. 6 (2006) 24–28.
[15] T. Ohno, M. Akiyoshi, T. Umebayashi, K. Asai, T. Mitsui, M. Matsumura, Appl. Catal. A 265 (2004) 115–121.
[16] N. Sharotri, D. Sud, New. J. Chem. 39 (2015) 2217–2223.
[17] C. Das, P. Roy, M. Yang, H. Jha, P. Schmuki, Nanoscale 3 (2011) 3094–3096.
[18] I.S. Cho, C.H. Lee, Y. Feng, M. Logar, P.M. Rao, L. Cai, D.R. Kim, R. Sinclair, X. Zheng, Nat. Comm. 4 (2013) 1723.
[19] (a) N. Mathews, M.C. Jacome, C. Angeles-Chavez, J.T. Antonio, J. Mater. Sci.: Mater. Electron. 26 (2015) 5574–5584;
(b) C.L. Luu, Q.T. Nguyen, S.T. Ho, Adv. Nat. Sci.: Nanosci. Nanotechnol. 1 (2010) 015008.
[20] L. Cai, I.S. Cho, M. Logar, A. Metha, J. He, C.H. Lee, P.M. Rao, Y. Feng, J. Wilcox, F.B. Prinz, X. Zheng, Phys. Chem. Chem. Phys. 16 (2014) 12299–12306.
[21] (a) M.M. Momeni, Y. Ghayeb, J. Alloy. Comp. 637 (2015) 393–400;
(b) H. Zhu, J. Tao, X. Dong, J. Phys. Chem. C 114 (2010) 2873–2879.
[22] Q.R. Deng, X.H. Xia, M.L. Guo, Y. Gao, G. Shao, Mater. Lett. 65 (2011) 2051–2054.
[23] C.W. Moon, S.Y. Lee, W. Sohn, D.M. Andoshe, D.H. Kim, K. Hong, H.W. Jang, Part. Part. Syst. Charact. 34 (2017) 1600340.
[24] S. Piskunov, O. Lisovski, J. Begens, D. Bocharov, Y.F. Zhukovskii, M. Wessel, E. Spohr, J. Phys. Chem. C 119 (2015) 18686–18696.
[25] G. Yan, M. Zhang, J. Hou, J. Yang, Mater. Chem. Phys. 129 (2011) 553–557.
[26] J. Chung, J.W. Chung, S.-Y. Kwak, Phys. Chem. Chem. Phys. 17 (2015) 17279–17287.
[27] (a) P.V.R.K. Ramacharyulu, D.B. Nimbalkar, J.P. Kumar, G.K. Prasad, S.-C. Ke, RSC Adv. 5 (2015) 37096–37101;
(b) N. Li, X. Zhang, W. Zhou, Z. Liu, G. Xie, Y. Wang, Y. Du, Inorg. Chem. Front. 1 (2014) 521–525;
(c) P. Goswami, J.N. Ganguli, RSC Adv. 3 (2013) 8878–8888.
[28] (a) M. Lu, P. Pichat, Photocatalysis and Water Purification: from Fundamentals to Recent Applications, John Wiley & Sons, Weinheim, Germany, 2013;
(b) D.-D. Qin, X.-H. Wang, Y. Li, J. Gu, X.-M. Ning, J. Chen, X.-Q. Lu, C.-L. Tao, J. Phys. Chem. C 120 (2016) 22195–22201.
[29] (a) J.A. Rengifo-Herrera, E. Mielczarski, J. Mielczarski, N.C. Castillo, J. Kiwi, C. Pulgarin, Appl. Catal. B: Envrion. 84 (2008) 448–456;
(b) T. Hirakawa, Y. Nosaka, J. Phys. Chem. C 112 (2008) 15818–15823.
[30] Y.-H. Lin, S.-H. Chou, H. Chu, J. Nanopart. Res. 16 (2014) 2539.
[31] D.M. Andoshe, S. Choi, Y.-S. Shim, S.H. Lee, Y. Kim, C.W. Moon, D.H. Kim, S.Y. Lee, T. Kim, H.K. Park, M.G. Lee, J.M. Jeon, K.T. Nam, M. Kim, J.K. Kim, J. Oh, H.W. Jang, J. Mater. Chem. A 4 (2016) 9477–9485.
[32] W. Yang, Y. Yu, M.B. Starr, X. Yin, Z. Li, A. Kvit, S. Wang, P. Zhao, X. Wang, Nano Lett. 15 (2015) 7574–7580.
[33] G. Kresse, J. Hafner, Phys. Rev. B 47 (1993) 558–561.
[34] C. Freysoldt, J. Neugebauer, C.G. Van de Walle, Phys. Rev. Lett. 102 (2009) 016402.
[35] Y. Kumagai, F. Oba, Phys. Rev. B 89 (2014) 195205.
[36] B.M. Kayes, H.A. Atwater, N.S. Lewis, J. Appl. Phys. 97 (2005) 114302.
[37] G. Liu, L. Wang, C. Sun, X. Yan, X. Wang, Z. Chen, S.C. Smith, H.-M. Cheng, G.Q. Lu, Chem. Mater. 21 (2009) 1266–1274.
[38] G. Liu, L.-C. Yin, J. Wang, P. Niu, C. Zhen, Y. Xie, H.-M. Cheng, Energy Environ. Sci. 5 (2012) 9603–9610.
[39] (a) I.S. Cho, J. Choi, K. Zhang, S.J. Kim, M.J. Jeong, L. Cai, T. Park, X. Zheng, J.H. Park, Nano Lett. 15 (2015) 5709–5715;
(b) G. Ai, R. Mo, H. Li, J. Zhong, Nanoscale 7 (2015) 6722–6728;
(c) A. Sasinska, T. Singh, S. Wang, S. Mathur, R. Kraehnert, J. Vac. Sci. Technol. A 33 (2015) 01A.
[40] Z. Chen, H.N. Dinh, E. Miller, Photoelectrochemical Water splitting, Springer Briefs in Energy vol. 49, Springer, New York, USA, 2013.
[41] (a) R.E. Hummel, Electronic Properties of Materials, Springer Science & Business Media, NY, USA, 2011;
(b) B.G. Streetman, S. Banerjee, Solid State Electronic Devices vol. 4, Prentice Hall, New Jersey, 2000;
(c) R.H. Bube, Electrons in Solids: an Introductory Survey, Academic press, NY, USA, 1992;
(d) W. Choi, A. Termin, M.R. Hoffmann, J. Phys. Chem. 98 (1994) 13669–13679.
[42] R. Sharma, P.P. Das, M. Misra, V. Mahajan, J.P. Bock, S. Trigwell, A.S. Biris, M.K. Mazumder, Nanotechnology 20 (2009) 075704.
[43] G. Wang, H. Wang, Y. Ling, Y. Tang, X. Yang, R.C. Fitzmorris, C. Wang, J.Z. Zhang, Y. Li, Nano Lett. 11 (2011) 3026–3033.
[44] T. Hirakawa, Y. Nosaka, J. Phys. Chem. C 112 (2008) 15818–15823.